Simulation of ductile crack propagation in dual-phase steel

G. Gruben*, O.S. Hopperstad and T. Børvik

Structural Impact Laboratory (SIMLab), Centre for Research-based Innovation (CRI) and Department of Structural Engineering, Norwegian University of Science and Technology, Rich. Birkelands vei 1A, NO-7491 Trondheim, Norway

Abstract

The modified Mohr-Coulomb and the extended Cockcroft-Latham fracture criteria are used in explicit finite-element simulations of ductile crack propagation in a dual-phase steel sheet. The sheet is discretized using tri-linear solid elements and the element erosion technique is used to model the crack propagation. The numerical results are compared to quasi-static experiments conducted with five types of specimens (uniaxial tension, plane-strain tension, in-plane shear, 45° and 90° modified Arcan) made from a 2 mm thick sheet of the dual-phase steel Docol 600DL. The rate-dependent J_2 flow theory with isotropic hardening was used in the simulations. The predicted crack paths and the force-displacement curves were quite similar in the simulations with the different fracture criteria. Except for the 45° modified Arcan test, the predicted crack paths were in good agreement with the experimental findings. The effect of using a high-exponent yield function in the prediction of the crack path was also investigated, and it was found that this improved the crack path prediction for the 45° modified Arcan test. In simulations carried out on finite element models with a denser spatial discretization, the prediction of localized necking and crack propagation was in better accordance with the experimental observations. In four out of five specimen geometries, a through-thickness shear fracture was observed in the experiments. By introducing strain softening in the material model and applying a dense spatial discretization, the slant fracture mode was captured in the numerical models. This did not give a significant change in the global behaviour as represented by the force-displacement curves.

Keywords: Crack propagation; Dual phase steel; Ductile fracture; Finite element method; Material instability

* Corresponding author. Tel.: + 47-73-59-46-87; fax: + 47-73-59-47-01

E-mail address: gaute.gruben@ntnu.no (G. Gruben).

1 Introduction

Various approaches exist for predicting fracture initiation and crack propagation numerically. In problems involving ductile materials, the failure criteria typically express the deterioration of the material by an accumulative damage variable. The damage variable can be coupled with the constitutive relation of the material as in porous plasticity models, e.g. Shima and Oyane (1976), Gurson (1977) and Rousselier (1987), or continuum damage mechanics models such as Lemaitre and Chaboche (1990) and Lemaitre (1992). Another approach is utilized in the uncoupled models, e.g. Cockcroft and Latham (1968), Wilkins (1980) and Johnson and Cook (1985), where the damage has no effect on the constitutive behaviour. As most ductile failure criteria depend on the deformation history of the material, it is crucial that the numerical model is capable of describing the deformation processes taking place before fracture in order to make good predictions of fracture initiation and crack propagation. Stochastic variations of the material characteristics may also influence the results to various degrees depending on the problem at hand, see e.g. Fyllingen et al. (2007) and Dørum et al. (2009). A range of techniques exists for simulating crack propagation with the Finite Element (FE) method, such as node splitting (Kazutake, 1999; Komori, 2005), cohesive elements (Needleman, 1990; Tvergaard and Hutchinson, 1996; Tvergaard, 2001), remeshing adaptivity (Bouchard et al., 2000; Mediavilla et al., 2006) and the extended finite element method (Areias, 2006; Fagerström and Larsson, 2006). A method that is relatively simple, robust and has proven to work well in problems involving large deformations is the element erosion technique (Xue and Wierzbicki, 2008; Fagerholt et al., 2010; Kane et al., 2011). In this technique, the load-carrying capacity of the element is set to zero when the fracture criterion is met at one or more integration points.

In this study, the modified Mohr-Coulomb criterion presented by Bai and Wierzbicki (2010) and the extended Cockcroft-Latham criterion presented by Gruben et al. (2012a) are used in explicit finite-element simulations of ductile crack propagation in a low-strength, high-hardening dual-phase steel, and the results are compared to experimental data reported by Gruben et al. (2011). The fracture criteria have been calibrated and assessed with respect to fracture initiation for this material by Gruben et al. (2012a), under the assumption of J_2 flow theory. In this study, the fracture criteria are evaluated with respect to fracture propagation by use of FE analyses in combination with the element erosion technique. It is shown that the fracture criteria neither give large variations in the predicted crack paths nor in the force-

displacement curves. Additionally, the effect of the shape of the yield surface on the fracture propagation is studied. It is shown that for moderate changes in the yield surface, the effects on the crack paths and the force-displacement curves are small in the single-mode fracture tests. In the mixed-mode fracture test, a higher exponent of the yield surface gives a better prediction compared to the experiments. The effects of mesh refinement and coupled damage have also been studied. Mesh refinement leads to more rapid strain localization, followed by a more rapid global failure. By including strain softening in the dense-mesh FE models, it is possible to numerically predict slant fracture, but this has virtually no influence on the global response in terms of force-displacement curves.

2 Experiments

Gruben et al. (2011) carried out experiments on specimens in the low range of stress triaxiality. A description of the material and test set-ups is briefly repeated here, together with supplementary information on the material from more recent studies. Finally, a detailed discussion of the crack propagation in the various test specimens is given.

The material used was a low-strength, high-hardening, steel of type Docol 600DL. This is a dual-phase steel where the ferrite gives the formability and the martensite gives the strength. The chemical composition of the material is given in Table 1. Fig. 1 displays the geometry of the four different specimen types used (uniaxial tension, plane-strain tension, in-plane shear and modified Arcan) in the rectangular coordinate system defined by the base vectors $(\mathbf{e}_X, \mathbf{e}_Y, \mathbf{e}_Z)$. Fig. 2 displays the test set-up for the modified Arcan tests. Here the angle β was set to respectively $45°$ and $90°$. All specimens were cut from a 2 mm thick steel sheet with the longitudinal axis in the rolling direction, except the uniaxial tension tests, which also were cut $45°$ and $90°$ to the rolling direction in order to determine the anisotropy of the material. The experiments were conducted under displacement control at room temperature with pre-necking strain rates in the vicinity of 10^{-3} s^{-1}. The force and displacement were measured in each test by the hydraulic test machine. In addition, an in-house digital image correlation (DIC) code (Fagerholt, 2012) was used to measure the displacement fields and to calculate the strain fields. The force-displacement $(F-u)$ curves from typical tests in the five set-ups are given in Fig. 3. The fracture characteristics of the material were determined at the through-thickness centre of the specimens by a hybrid experimental-numerical procedure, and

at the surface of the specimens by utilizing an experimental procedure based on optical measurements. It was found that the variation in ductility as function of stress state was rather small for the stress states investigated and that the range in measured fracture strain was somewhat larger on the surface than in the centre. It was further argued that for calibration of 3D solid elements the data from the through-thickness centre should be used, while for plane-stress elements the data from the surface are relevant. A more recent study of the fracture surfaces of the specimens by scanning electron microscopy (Gruben et al., 2012a) showed that the governing fracture mechanism in the tests was nucleation, growth and coalescence of microvoids. This observation is supported by a study comprising formability tests on material from the same batch (Gruben et al., 2012b). The formability tests revealed that the material displays a significantly lower ductility in plane-strain tension than in uniaxial tension and biaxial tension.

Three parallels of the uniaxial tension test were performed on specimens cut $0°$, $45°$ and $90°$ to the rolling direction (a total of nine tests). Only small variations could be observed in the force-displacement curves, and the plastic flow was assumed to be nearly isotropic (Gruben et al., 2011). The force-displacement curves from two typical tests in the rolling direction are displayed in Fig. 3. From the hardening law fitted to one of the tests in the rolling direction, see Equation (1) below, the Considère criterion estimates diffuse necking to take place at an equivalent plastic strain of 0.18 (ignoring strain rate effects). By using Hill's criterion, localized necking is predicted at an equivalent plastic strain of 0.31. The equivalent strain at fracture, henceforth called the fracture strain, was calculated from DIC measurements and found to be 0.82. The characteristic element size used in the DIC analysis was 0.9 mm. This value of the fracture strain refers to fracture initiation and is valid for the surface of the specimen. The fracture strain has also been determined by calculating the logarithmic strain from the area reduction at fracture, i.e. $\varepsilon_f = \ln(A_0 / A_f)$ (Johnsen, 2009). Here A_0 is the initial cross-section area, and A_f is the projection of the cross-section area in the $\mathbf{e}_X$ plane at global failure. This approach resulted in a fracture strain $\varepsilon_f = 0.80$ for the same specimen. For the nine tests an average fracture strain $\varepsilon_f = 0.81$ with a standard deviation of 0.03 was found from the area reduction measurement. This indicates that the material is isotropic also with respect to fracture. From the finite element analysis conducted by Gruben et al. (2011), it was found that the equivalent plastic strain at fracture is larger at the centre of the specimen. Here it is estimated to 0.85 by a finite element analysis using 3D solid elements with a

characteristic size of 0.38 mm. This simulation did however not capture the through-thickness shear bands observed in the specimens during testing. Experimentally the crack appeared within these shear bands in all nine tests, but three different modes were observed, see Fig. 4(a-c). The first mode is a slant fracture where the fracture plane is approximately $43°$ to $\mathbf{e}_Z$, see Fig. 4(b), with in-plane direction parallel to $\mathbf{e}_Y$, as illustrated in Fig. 4(c). Only one of the nine tests exhibited this mode. The second mode is a double through-thickness shear mode, or a V-mode; see Fig. 4(b). The V-mode displayed in-plane localization inclined approximately $22°$ in all three tests where it appeared; cf. specimen 2 in Fig. 4(c). The third mode is a combination of the two first modes, and was observed in five tests. In all the tests fracture initiated at the in-plane centre of the neck and propagated to the edges in less than 0.5 s corresponding to a actuator displacement increment $\Delta u = 0.017$ mm.

In the plane-strain tension tests, fracture initiated in the in-plane centre of the specimens and propagated roughly perpendicular to the loading direction; see Fig. 4(d). At the centre of the specimen, a rough surface was observed, but shear-lips were present also in this area, as illustrated in Fig. 4(d). A slant fracture mode occurred as the crack propagated towards the edges, as displayed in Fig. 4(d). As seen in Fig. 3, global failure occurred approximately $\Delta u \approx 0.47$ mm after fracture initiation.

The in-plane shear tests displayed a flat crack surface through the sheet thickness as illustrated in Fig. 4(e). Due to rotation of the material during the test, the crack surface was rotated approximately $22°$ with respect to $\mathbf{e}_X$, as displayed in Fig. 4(f). The fracture mode was the same in both tests, and global failure occurred in the instant that fracture initiated. From the force-displacement curves in Fig. 3, a small drop in force is observed in the last part of the curve. This may be due to a combination of material softening and a small reduction of the shear area.

The two Arcan-45 tests were exposed to a mixed-mode loading resulting in a curved crack path as displayed in Fig. 5(a). Fracture initiated in the notch root in a V-mode at a displacement $u \approx 7$ mm, but after less than 1 mm propagation it turned into a slant fracture mode, see Fig. 5(b). In both tests the crack then propagated uniformly in this mode until $u \approx 11.5$ mm. Here the crack got arrested and did not propagate further until the specimen failed completely at $u \approx 12.5$ mm. In this last $1/10$ of the crack path, in-plane shear localization occurred and produced a flat-fracture mode similar to the one observed in the in-plane shear tests, see Fig. 5(a) and Fig. 5(b). The point of fracture initiation can be seen in the force-

displacement curve in Fig. 3 as a sudden drop in the force level when $u \approx 7$ mm, while the in-plane shear failure can be seen as the drop in force at $u \approx 12.5$ mm. At $u \approx 10$ mm, the force curve flattens out. This may be due to a kinematic artefact stemming from the rotation of the specimens and the brackets.

For the Arcan-90 tests, fracture initiated in the centre of the notch and propagated in a direction nearly parallel to $\mathbf{e}_Y$, as displayed in Fig. 5(c). In both tests, the crack was in a V-mode at first. The tests exhibited this mode as the crack propagated approximately 2 mm and 5 mm, respectively, as displayed in Fig. 5(d). The crack then switched to a slant fracture mode. In one of the tests, the crack propagated in the same slant fracture mode until global failure, while in the other test the crack switched to the other shear band halfway through the specimen, see Fig. 5(d). As can be seen from the force-displacement curves in Fig. 3, the force level flattens out in a similar way as in the Arcan-45 tests in the last part of the curve before global failure. From the DIC analysis it was observed that the crack propagation velocity decreased in the final stages of the test. The reduction of the crack propagation velocity might be due to the rotation of the specimens and brackets.

3 Numerical modelling

The spatial discretizations and boundary conditions of the FE models in this study are based on the models described by Gruben et al. (2011). In this study the simulations were run with the explicit solver of LS-DYNA version 971 (LSTC, 2007) with the constitutive model and fracture criteria described below implemented as user-defined material models. The modified Arcan specimens were discretized with a random element distribution in the $\mathbf{e}_Z$ plane, while the other models had a structured mesh. The discretizations are displayed in Fig. 6. In all these models nine elements were used over the thickness, giving an initial element height of 0.22 mm. Table 2 gives the characteristic element size in the different models. In addition, models of the uniaxial tension, plane-strain tension and in-plane shear tests with finer discretizations were made. Fig. 7 illustrates the discretization of the uniaxial tension specimen with finer a mesh. A small geometric trigger was used in this model to obtain diffuse necking in the centre of the zone with finer mesh. Since the elements undergo large deformations before fracture, the initial aspect ratio of the elements in the fracture zone of the uniaxial tension and plane-strain tension dense-mesh models were made so that the elements had a nearly cubic shape at the point of failure. The final density of the mesh in the dense-mesh

models was found at the point where a denser mesh did not produce a significant change in the fracture mode. As stated by Belytschko et al. (2000), solutions of shear-band localization problems converge slowly with mesh refinement. Thus, the FE models with the fine discretization have 18 elements in the thickness direction, corresponding to an initial height of 0.11 mm. The characteristic element sizes of the dense-mesh FE models are summed up in Table 2. The modified Arcan tests were not simulated with denser mesh, since the computational time was extensive. The elements used in the coarse-mesh FE models in Sections 5.1 and 5.2 below were eight-node, trilinear solids with selectively reduced integration (Type 2 in LS-DYNA). Due to computational costs, eight-node, trilinear solid elements with reduced integration (Type 1 in LS-DYNA) were utilized in the FE models in Section 5.3 below. The applied loading rate was increased by a factor 10^5 to maintain a reasonable computational time. Control with the kinetic energy and comparisons with simulations using implicit time-integration showed that this time scaling is admissible. The reference strain rate $\dot{\varepsilon}_0$ in Equation (1) was equally increased to maintain the correct proportions due to the time scaling.

3.1 Constitutive relation

3.1.1 Work hardening

The work hardening of the material was fitted to the extended Voce rule with a multiplicative viscosity-hardening law as (Gruben et al., 2012a)

$$\bar{\sigma} = \left(\sigma_0 + \sum_{i=1}^{3} Q_i \left(1 - \exp(-C_i \bar{\varepsilon}^p)\right) \right) \cdot \left(1 + \frac{\dot{\bar{\varepsilon}}^p}{\dot{\varepsilon}_0} \right)^q \tag{1}$$

where $\bar{\sigma}$ is the equivalent stress defined by the yield criterion, $\bar{\varepsilon}^p$ is the equivalent plastic strain conjugate in power to the equivalent stress, σ_0 is a material parameter representing the yield stress, and Q_i and C_i $(i = 1, 2, 3)$ are material parameters governing in turn the primary, secondary and tertiary hardening of the material. The parameters q and $\dot{\varepsilon}_0$ are material constants defining the strain-rate sensitivity of the material. The strain-rate sensitivity was not investigated experimentally for this material, but reasonable values for dual-phase steels (Tarigopula et al., 2006; Curtze, 2009) were used. The hardening parameters were found by a fit of the Cauchy stress – logarithmic plastic strain curve from the uniaxial tension test up to

diffuse necking, and by inverse modelling for large strains using the uniaxial tension and in-plane shear tests. Table 3 gives the work-hardening parameters for the material.

3.1.2 Yield function

The plastic flow of the material was found to be virtually isotropic, and the modelling in the previous studies (Gruben et al., 2011; Gruben et al., 2012a) was done by the J_2 flow theory. It was discussed by Gruben et al. (2011) that a high exponent yield function might give a better description of the material's yield surface. As part of this study, a high-exponent, isotropic yield function, as proposed by Hershey (1954), was used to investigate the effect of the shape of the yield surface. The equivalent stress is expressed as

$$\bar{\sigma} = \sqrt[m]{\frac{1}{2}\left(\left|\sigma_I - \sigma_{II}\right|^m + \left|\sigma_{II} - \sigma_{III}\right|^m + \left|\sigma_{III} - \sigma_I\right|^m\right)} \tag{2}$$

where σ_i, $i = I, II, III$ are the principal stresses ordered so that $\sigma_I \geq \sigma_{II} \geq \sigma_{III}$, and $m \geq 1$ controls the curvature of the yield surface. The Tresca yield surface is obtained with $m = 1$ while $m = 2$ gives the von Mises yield surface. The von Mises yield surface is again found at $m = 4$ and the Tresca yield surface at $m \to \infty$ (Hosford, 1972). It is noted that for m values other than 2 and 4, J_3 dependency is introduced. Previous studies (Hutchinson, 1964a, b) have indicated that the yield surface of BCC materials is closer to the von Mises yield surface, while for FCC materials it is closer to the Tresca yield surface. The Docol 600DL material mainly consists of ferrite (BCC) and martensite (BCT).

3.1.3 Damage coupling

In general, material softening is the macroscopic effect of adiabatic heating or micro-porosity during plastic deformation. A phenomenological model introducing material softening due to micro-porosity can be expressed as (de Borst, 2004)

$$\boldsymbol{\sigma} = \tilde{\boldsymbol{\sigma}}\left(1 - \omega\right) \tag{3}$$

where $\boldsymbol{\sigma}$ is the Cauchy stress tensor, $\tilde{\boldsymbol{\sigma}}$ is the effective Cauchy stress tensor assumed to act on the un-deteriorated matrix material and ω is the scalar damage variable. In this study, the damage variable introduced by Xue and Wierzbicki (2008), was applied, i.e. $\omega = D^{\beta}$, where $0 \leq D \leq D_C$ is the accumulated damage parameter from either Equation (8) or (9), and $\beta > 1$ is the weakening exponent controlling the influence of the accumulated damage. Further, the D_C value in the simulations involving coupled damage was set to 0.995 in this study. If D is

larger than the critical value, D_C, the element loses its load-carrying capacity and is eroded. In this study, it was chosen that the element is eroded if D_C is reached in one integration point, even if the element has several integration points. Note that the limiting value $\beta \to \infty$ leads to uncoupled damage. The damage coupling procedure used is similar to the methodology described by de Borst (2004), i.e. $\tilde{\boldsymbol{\sigma}}$ is substituted for $\boldsymbol{\sigma}$ in all constitutive relations.

3.2 Fracture criteria

3.2.1 The modified Mohr-Coulomb criterion

The Mohr-Coulomb fracture criterion is expressed in the stress space as

$$\tau + c_1 \sigma_n = c_2 \tag{4}$$

where τ is the shear stress and σ_n is the normal stress at fracture on the critical plane of the material. The material constant c_1 is often referred to as the friction, while c_2 is the cohesion. An alternative formulation of the Mohr-Coulomb criterion is (Gruben et al., 2012a)

$$\frac{\phi\left(3\sigma^*\sqrt{3+\mu^2} - 3 - \mu\right) + 6}{3\sqrt{3+\mu^2}}\bar{\sigma}_{VM} = C \tag{5}$$

where

$$\phi = \frac{2c_1}{\sqrt{1+c_1^2}+c_1},\ 0 \le \phi \le 1, \quad \text{and} \quad C = \frac{2c_2}{\sqrt{1+c_1^2}+c_1} > 0$$

Here $\bar{\sigma}_{VM}$ is the von Mises equivalent stress, i.e. $m = 2$ in Equation (2), while σ^* is the stress triaxiality and μ is the Lode parameter (Lode, 1926), defined as

$$\sigma^* = \frac{\sigma_I + \sigma_{II} + \sigma_{III}}{3\bar{\sigma}_{VM}}, \quad \mu = \frac{2\sigma_{II} - \sigma_I - \sigma_{III}}{\sigma_I - \sigma_{III}} \tag{6}$$

A modified version of the Mohr-Coulomb criterion for ductile fracture was introduced by Bai and Wierzbicki (2010). This modified version utilizes a calculated fracture strain that depends on the stress state, $\bar{\varepsilon}_f^p = \bar{\varepsilon}_f^p(\boldsymbol{\sigma})$. Gruben et al. (2012a) estimated the fracture strain $\bar{\varepsilon}_f^p$ by replacing $\bar{\sigma}_{VM}$ in Equation (5) with the expression for the work hardening, Equation (1). In

the case of a Hershey yield function, a modification is needed to have consistency between the constitutive relation and the fracture criterion. It can be shown that the relation between the von Mises equivalent stress, $\bar{\sigma}_{VM}$, and the Hershey effective stress, $\bar{\sigma}$, from Equation (2) is expressed by the Lode parameter, μ, and the exponent m as

$$\bar{\sigma}_{VM} = \frac{\sqrt{3+\mu^2}}{\sqrt[m]{\frac{(1+\mu)^m + (1-\mu)^m + 2^m}{2}}} \bar{\sigma} \tag{7}$$

In order to estimate the fracture strain, $\bar{\varepsilon}_f^p$, the equivalent stress, $\bar{\sigma}$, in Equation (7) is replaced with the expression from Equation (1), and the resulting expression for $\bar{\sigma}_{VM}$ is inserted into Equation (5). The modified Mohr-Coulomb criterion (MMC) may then be expressed as a damage parameter

$$D = \int_0^{\bar{\varepsilon}^p} \frac{d\bar{\varepsilon}^p}{\bar{\varepsilon}_f^p} \tag{8}$$

where fracture initiates when D equals unity. It is noted that the modified Mohr-Coulomb criterion suggested for application by Bai and Wierzbicki (2010) incorporated four fracture parameters. Only the two fracture parameters stemming from the stress-based Mohr-Coulomb criterion are applied in this study.

3.2.2 The extended Cockcroft-Latham criterion

The extended Cockcroft-Latham (ECL) criterion was introduced by Gruben et al. (2012a), and is expressed as

$$D = \frac{1}{W_C} \int_0^{\bar{\varepsilon}^p} \left\langle \phi \frac{\sigma_I}{\bar{\sigma}} + (1-\phi) \left(\frac{\sigma_I - \sigma_{III}}{\bar{\sigma}} \right) \right\rangle^{\gamma} \bar{\sigma} d\bar{\varepsilon}^p \tag{9}$$

where $\langle \cdot \rangle$ is the Macaulay brackets and $W_C \geq 0$, $0 \leq \phi \leq 1$ and $\gamma \geq 0$ are the fracture parameters. The overall ductility of the material is defined through W_C, while ϕ weights the influence of the major principal stress and the maximum shear stress, and γ controls the strength of the stress-state dependence. Fracture is assumed to initiate when the damage parameter, D, reaches the critical value, D_C. For uncoupled damage D_C may be set to unity with no loss of generality, while for coupled damage this value determines the material softening before failure. The ECL criterion is a generalization of several other fracture

criteria. By setting $\gamma = 1$ an integral-based representation of the Mohr-Coulomb criterion is obtained, where the special case $\gamma = 1,\ \phi = 0$ gives the Integral-based Tresca (IT) criterion (Gruben et al., 2012a). The combination $\gamma = \phi = 1$ gives the Cockcroft-Latham (CL) criterion (Cockcroft and Latham, 1968), while $\gamma = \phi = 0$ gives the Freudenthal criterion (Freudenthal, 1950).

4 Calibration of fracture criteria

The fracture criteria presented in Section 3.2 were calibrated by Gruben et al. (2012a) under the assumption of J_2 flow utilizing the data from the centre of the specimens obtained by the hybrid experimental-numerical procedure conducted by Gruben et al. (2011). These calibrations were based on FE models with coarse mesh similar to the ones described in the beginning of Section 3, see Table 2. More calibrations based on the coarse-mesh FE models have been carried out with the Hershey yield function, using the same procedures as Gruben and co-workers (2011; 2012a). The in-plane shear test and the uniaxial tension test were used to calibrate the MMC, CL and IT criteria. For the ECL criterion, additional data from the plane-strain tension test were used, and the criterion was calibrated for yield functions with $m = 2, 6, 8$. Table 4 gives the results from the calibrations. The fracture strain loci in the $(\sigma^*, \bar{\varepsilon}_f^p)$ space defined by the various fracture criteria, assuming proportional loading and plane-stress, are displayed in Fig. 8 for $m = 2$ (J_2 flow theory) and $m = 8$. The exponent m in the yield function does affect the predicted fracture strain, especially for the MMC and the ECL criteria. For the MMC criterion, the $m = 8$ calibration led to a lower value of ϕ, which again led to lower dependency of the stress triaxiality, cf. Equation (5). In the ECL calibrations, it is seen from Table 4 that a higher value of m leads to a higher value of the stress-state dependency parameter, γ, which is followed by a larger range in the predicted fracture strain as function of stress state.

The dense-mesh FE simulations, with and without damage softening, displayed increased strain gradients compared to the coarse-mesh FE simulations. Accordingly, the fracture strain in the dense-mesh FE simulations increased, and it was found that the increase in ductility was approximately 7 % in the case without softening. To account for this, a new set of input parameters had to be determined for the dense-mesh FE models. Simulations of

the uniaxial tension test were used to scale the parameters in the material model with the ECL criterion and the von Mises yield surface. It was assumed that the weighting between the major principal stress and the maximum shear stress, ϕ, as well as the stress-state dependence, γ, was unaffected by mesh refinement and damage softening. Thus, the only fracture parameter to be adjusted was the ductility parameter, W_C. It was found that the relation between D and $\bar{\varepsilon}^p$ in the uniaxial tension test simulation with uncoupled damage was given a good approximation by $D(\bar{\varepsilon}^p) = (\bar{\varepsilon}^p / \bar{\varepsilon}_f^p)^{1.25}$. Since W_C is used in normalizing D, cf. Equation (9), the W_C value was scaled by a factor $1.07^{1.25}$ to account for the increased fracture strain due to mesh refinement. For the case with dense mesh and coupled damage the calibration was more involved. Here it was postulated that the plastic work per volume up to fracture, $\int_0^{\bar{\varepsilon}_f^p} \bar{\sigma} d\bar{\varepsilon}^p$, is invariant to material softening. In order to ensure this, the work-hardening parameters, σ_0, Q_i and C_i, had to be adjusted in addition to the ductility parameter, W_C, for a given weakening exponent, β. This can be done by inverse modelling. However, a good estimate can be made based on the $D(\bar{\varepsilon}^p)$ relation in the uncoupled case. By using the latter approach, the work-hardening curve for the damage softening material was readily produced by trial and error in MATLAB (2009). For a given β and a given trial value for the fracture strain, an optimization of the work-hardening curve for the softened material was conducted. The hardening parameters were optimized to the $\bar{\sigma} - \bar{\varepsilon}^p$ curve of the undamaged material in the interval $\bar{\varepsilon}^p \in [0, 0.5]$, i.e. assuming no influence of damage on the stress-strain behaviour in this strain range. Then a control of the plastic work was carried out. If the plastic work up to fracture of the softened material was the same as the plastic work of the unsoftened material, the fracture strain and the hardening parameters were considered admissible. If the solution is inadmissible, the trial value of the fracture strain is changed and the procedure is repeated. The resulting work-hardening curve for $\beta = 6$ is compared with the work-hardening curve of the material without damage softening in Fig. 9(a). The material with damage softening exhibits an increase in fracture strain of 13 % compared to the case with dense-mesh and uncoupled damage. Accordingly, the ductility parameter, W_C, was increased by a factor $1.13^{1.25}$. The weakening exponent, β, was found by trial and error. Here, a comparison of the simulated and experimental force-displacement curves from the uniaxial tension and in-plane shear tests were used, and $\beta = 6$ was found to give reasonable

results for both tests. The work-hardening parameters for $\beta = 6$ are summed up in Table 3, while the fracture parameters for the dense-mesh calibrations with and without damage softening are given in Table 4.

The damage evolution of the Docol 600DL material has not been studied experimentally. However, Avramovic-Cingara et al. (2009) determined the area void fraction as function of thickness strain for uniaxial tensile tests cut from a comparable DP600 steel-sheet. They found that the evolution of the area void fraction had an exponential shape with initial value 0.001 and final value 0.013. The near linear shape of $D(\bar{\varepsilon}^p)$ shown in Fig. 9(b) is not coherent with the evolution of the area void fraction in the comparable DP600 steel. On the other hand, the $D^\beta(\bar{\varepsilon}^p)$ curve from the damage softening calibration displays an exponential shape more similar to the evolution of the void area fraction. Another aspect of the damage-softening modelling in this study is the value of D_C. This value should represent the total damage on the material from microvoids, accumulation of micro-stresses at defects, and breaking of bonds. The study of Avramovic-Cingara et al. (2009) indicated that the microvoids contribution to D_C is very small, and in this perspective $D_C \approx 1$ is very large. This value is however used here, since the objective is to show how damage softening influences the numerical simulations. For other studies, a lower value of D_C should be considered.

5 Simulation of crack propagation

5.1 Effect of fracture criterion

The effect of the fracture criterion on the crack propagation is presented in the following for the case of the coarse-mesh models, J_2 flow theory and uncoupled damage. The influence of the fracture criterion on the crack path in the five different tests is displayed in Fig. 10, which shows plots from the final stage of the simulation for each case. The displacement, u, corresponding to each plot is given in the figure. In the simulations of the uniaxial tension, plane-strain tension and modified Arcan tests, the elements in the thickness direction were deleted in a tunnelling mode; an example from the Arcan-45 test is given in Fig. 11(a). In the in-plane shear test all the elements through the thickness were deleted almost simultaneously.

The location of fracture initiation in the in-plane centre of the specimen was captured in the uniaxial and plane-strain tension tests by all fracture criteria, and the in-plane crack paths were similar to the experimental ones. Fracture initiates at the displacement where a significant drop in force level occurs in the $F-u$ curves in Fig. 3. In the simulations of the uniaxial tension test this drop occurred at almost the same displacement for all fracture criteria and fits well with the experimental values. This is in accordance with the fracture initiation prediction of the criteria found by Gruben et al. (2012a). In the simulations of the plane-strain tension test, the MMC criterion gave an early drop in force level, while the IT criterion predicted a somewhat late drop. The fracture initiation was predicted well by the ECL and CL criteria compared to the experimental results. This is also in accordance with the results from Gruben et al. (2012a). However, the crack propagation velocities were somewhat low in all simulations of the uniaxial tension, plane-strain tension and modified Arcan tests compared to the experiments.

In the shear test, the global failure in the simulations occurred just after fracture initiation as observed in the tests. This can be seen in Fig. 3 where there is a sudden drop in the force level and no "tail" of $F-u$ curves. The displacement at global failure was slightly overestimated in the simulations with the MMC and CL criteria. As shown in Fig. 3, the experimental values are between the results from the simulations with the ECL and IT criteria. The angle between the crack path and $\mathbf{e}_X$ was approximately $21°$ in the simulations with the ECL and CL criteria and approximately $18°$ in those with the MMC and IT criteria. As illustrated in Fig. 4(f), this angle is approximately $22°$ in the experiment.

The displacement at final failure in the simulations of the Arcan-45 test was close to the experimental values, but the numerically obtained $F-u$ curves were not in agreement with the experimental curves after fracture initiation, as displayed in Fig. 3. Further, the simulation with the MMC criterion yielded an earlier drop in force level and a larger displacement at global failure than the simulations with the other criteria. Gruben et al. (2012a) showed that the fracture strain predicted by the MMC criterion at the assumed location of fracture initiation was larger than the experimentally determined value. In the present study, the drop in force level, which is related to fracture initiation, occurred significantly earlier in the simulation with the MMC criterion than in the experiments. This apparent paradox is explained by the fact that elements away from the root of the notch were eroded before the elements in the notch root when using the MMC criterion; see Fig. 11(b).

This is in contrast to the experiments and simulations with the other fracture criteria where the crack initiated in the notch root, as displayed in Fig. 11(a). The MMC criterion predicted a very high ductility for uniaxial tension and low ductility for plane-strain tension, as illustrated in Fig. 8(a). The elements first eroded by the MMC criterion were practically in a plane-strain tension stress state with stress triaxiality $\sigma^* \approx 0.58$ and Lode parameter $\mu \approx 0$. This is illustrated in Fig. 11(c-d) where contours of the stress triaxiality and the Lode parameter are plotted just before the first elements are eroded. In the simulations of the Arcan-45 tests, the MMC criterion gave an $F-u$ curve with qualitatively better shape than those from simulations using the other fracture criteria, as displayed in Fig. 3. This may be due to the bilinear crack trajectory predicted by the MMC criterion which is more similar to the experimental crack path than the crack paths predicted by the other criteria, cf. Fig. 5(a) and Fig. 10. The bilinear crack path in the MMC simulation stems from the low ductility predicted by the criterion in plane-strain tension, which in the early stages of crack propagation drives the crack in a different direction than the direction with the largest equivalent plastic strain.

In the simulations of the Arcan-90 test, the predicted crack paths using the various fracture criteria were very similar, as illustrated in Fig. 10. The fracture initiated in the root of the notch in all simulations, except in the simulation with the MMC criterion. Here elements with a certain distance away from the notch root were eroded first, as in the simulation of the Arcan-45 test; see Fig. 11(b). This premature erosion of elements led to an earlier drop in force level compared to the simulations with the other fracture criteria, as evident in Fig. 3. The simulation with the MMC criterion gave, however, a good prediction of the displacement at global failure, while the simulations with the other fracture criteria tended to overestimate this value.

5.2 Effect of exponent in yield function

Simulations were also carried out using the Hershey yield function given by Equation (2). Fig. 12 illustrates how the yield loci for $m=6$ and $m=8$ are placed between the von Mises yield locus $(m=2)$ and the Tresca yield locus $(m\to\infty)$. The cases $m=6,8$ were chosen since BCC materials have proven to be closer to the von Mises than the Tresca yield surface (Hutchinson, 1964a). Only results from the coarse-mesh FE models with the ECL criterion are presented in this section. Fig. 13 gives the results in terms of force-displacement curves. As can be seen, there is no notable difference when using a Hershey yield function in the

simulations of the uniaxial tension test. In the simulations of the plane-strain tension test, a higher exponent tended to decrease the peak force and the displacement at fracture initiation and global failure. The opposite trend was observed in the simulations of the in-plane shear test where a higher exponent slightly increased the peak force and gave a significant increase in the displacement at global failure. Further, in the simulations of the Arcan-45 test, the force-displacement curves up to fracture initiation were not altered for increasing m values, but the displacement at global failure was increased. The simulations of the Arcan-90 test gave a trend in the force-displacement curves similar to the one observed for the plane-strain tension test; an increase in m gave a decrease in peak force and displacement at global failure.

In all but the simulations of the Arcan-45 test, the J_2 flow theory gave good predictions of the in-plane crack paths. With the Arcan-45 test as an important exception, the in-plane crack trajectory was not changed in the simulations with a Hershey yield function. However, for the Arcan-45 test, the simulation with $m = 8$ gave a curved crack path that to a higher extent resembles the experimental result. The crack trajectory in the simulation with $m = 6$ ended between the crack paths obtained with $m = 8$ and J_2 flow theory, but closer to the latter as displayed in Fig. 14(a-c). The change in the crack path may explain the larger displacement at global failure for higher m values in these simulations.

In Fig. 14(d-f), a plot of the early stages of fracture is shown from the simulation with J_2 flow theory and the ECL criterion. The contours are equivalent plastic strain, stress triaxiality and Lode parameter. The elements that will be eroded later in the simulation are marked. From Fig. 14(e-f) it is evident that the stress triaxiality is higher and the absolute value of the Lode parameter is lower on the upper left-hand side of the crack path. Since the ECL criterion predicts lower ductility for higher hydrostatic stress and low absolute values of the Lode parameter, this indicates that both the hydrostatic and the deviatoric stress state drive the crack to the upper left side in this simulation. However, as seen in Fig. 14(d), the equivalent plastic strain is largest in the direction of the crack path. From this we may conjure that the direction of the crack path is governed by the equivalent plastic strain in the simulation with J_2 flow theory. In the case with high exponent ($m = 8$) shown in Fig. 14(g-i), it is clear that the stress triaxiality and the Lode parameter drive the crack path in a different direction than the equivalent plastic strain, in the same manner as in the simulations using J_2 flow theory. In this case, however, it is seen that the crack path is governed by the stress state

approximately the first $\frac{3}{5}$ of the total trajectory before it bends into the direction having the maximum equivalent plastic strain in the last part.

5.3 Effect of mesh refinement and slant shear fracture

The slant shear fracture seen in most of the experiments was not captured in the finite element simulations in the previous sections. The reason for this is bipartite; firstly the spatial discretizations used in the models are too coarse to capture this phenomenon. Secondly the classical elastic-plastic solid with a smooth yield surface does not predict shear-band localization at realistic levels of straining unless the material displays a very low work hardening (Hutchinson and Tvergaard, 1981; Needleman and Tvergaard, 1992). However, by introducing a yield surface vertex, non-normality or material softening, the critical strain to capture shear band localization is considerably lowered (Hutchinson and Tvergaard, 1981).

In order to investigate the effect of mesh refinement and slant shear fracture in the numerical analysis, additional simulations were carried out on models with finer discretization, J_2 flow theory and the ECL fracture criterion with and without coupled damage. As pointed out by Needleman (1988), the size of the shear band in the simulation is restricted by the element size. The shear-band width was not measured for the Docol 600DL material under quasi-static, isothermal loading, and the authors could not find data in the literature for a similar material deformed under similar loading. However, the final element size of the dense-mesh FE models (≈ 80 μm) may be in the vicinity of the experimental shear-band width, based on the experience from the study conducted by Solberg et al. (2007). In that study it was found that the width of adiabatic shear bands in three different types of Weldox steels were in the vicinity of $10-100$ μm, somewhat depending on the material.

The $F-u$ curves and the crack surfaces from the dense-mesh simulations of the uniaxial tension, plane-strain tension and in-plane shear tests are given in Fig. 15. Here the $F-u$ curves are compared with results from coarse-mesh FE analyses utilizing the ECL criterion, J_2 plasticity and reduced integrated elements. In the FE simulations of the uniaxial tension and plane-strain tension tests, the strain softening gave a pronounced through-thickness slant fracture as shown in Fig. 15. However, the $F-u$ curves were nearly identical to the curves from the dense-mesh, uncoupled damage FE simulations where no slant fracture was predicted. This is in accordance with the findings of Li et al. (2011). The crack in the uniaxial

tension simulation with coupled damage displayed an in-plane angle not unlike what was observed in the experiments, while the V-mode was not as pronounced as in the experimental tests. The simulation of the plane-strain tension test with coupled damage, on the other hand, displayed a more distinct slant fracture in the centre of the specimen than in the experiments. It is noted that the symmetry and anti-symmetry of the fracture surfaces observed in the uniaxial tension and plane-strain tension simulations disappear if for instance material inhomogeneity is introduced. However, since the slant fracture surfaces in the experiments had a stochastic nature, an exact match between the experimental and simulated fracture surface cannot be expected. The mesh refinement led to a lower displacement at fracture initiation. This can be explained by the increased strain gradient in the dense-mesh FE models which advances the through-thickness localization. The effect of strain softening was more pronounced on the $F-u$ curves of the shear test simulation than in the simulations of the other two tests. This is because the shear tests do not exhibit necking instability before fracture. The displacement at fracture in the experimental shear tests is $u_f \approx 3.5$ mm, which is between the displacement at fracture predicted by the simulations with a denser mesh using coupled and uncoupled damage, respectively. The fracture surface in the shear simulations was not influenced by mesh refinement or damage softening as can be seen in Fig. 15, and is similar to the fracture surface observed in the experiments.

6 Discussion

The crack trajectories in the simulations of the material tests with coarse mesh, i.e. uniaxial tension, in-plane shear and plane-strain tension were similar, independent of fracture criterion and yield function. The same yields for the simulations of the Arcan-90 test. The crack paths in all these tests are controlled by the geometry of the specimens and the test set-ups, so only small variations in the predicted crack paths were observed. The crack paths in the simulations of the mixed-mode Arcan-45 test, however, differed to a certain degree when the fracture criterion and yield function were changed. The combination of J_2 flow theory and the MMC fracture criterion gave a crack path initially governed by the stress state before it abruptly changed to the direction of the largest equivalent plastic strain, leaving a bilinear crack trajectory. The simulation in which the Hershey yield function with $m=8$ and the ECL criterion were used, gave a crack path that was a result of a competition between the stress and equivalent plastic strain fields in the specimen during the first part of the crack trajectory.

This led to a curved shape of the crack path in this region that resembled the experimental results. In the last part, the crack path propagated in the direction of the largest equivalent plastic strain, and formed a linear trajectory. All the other simulations of the Arcan-45 test gave a nearly linear crack path in the direction of largest equivalent plastic strain. These results show that the Arcan-45 test is more challenging than the other tests for evaluating fracture criteria with respect to crack propagation.

In the simulations of the uniaxial tension, plane-strain tension and modified Arcan tests, the displacement increment from fracture initiation to global failure, Δu, was large compared to the experiments. In the simulations of the plane-strain tension test, it can be seen from Fig. 3 and Fig. 15 that the displacement increment from fracture initiation to global failure is $\Delta u \approx 1.5$ mm and $\Delta u \approx 2.1$ mm in the simulations with coarse mesh in combination with selectively reduced (Section 5.1) and reduced integration (Section 5.3), respectively. The dense-mesh simulations gave $\Delta u \approx 1.3$ mm for both uncoupled and coupled damage, while the experiments had $\Delta u \approx 0.5$ mm. In the simulations of the uniaxial tension test, the same trend is observed in Fig. 3 and Fig. 15. Here the simulations with coarse mesh gave $\Delta u \approx 0.6$ mm and $\Delta u \approx 1.0$ mm for selective-reduced and reduced integration, respectively, $\Delta u \approx 0.3$ mm for the simulations with finer mesh, while $\Delta u < 0.02$ mm in the experiments. Since the damage is driven by plastic strain and the crack propagation is a sequence of fracture initiation in the eroded elements, the observations suggest that a large number of degrees of freedom should be used in the FE models to capture the crack propagation speed found experimentally. There was a significant effect when increasing the number of elements as well as when going from elements with selectively-reduced integration to reduced integration, whereas damage softening and prediction of slant fracture did not significantly influence the speed of the crack propagation in the simulations. The displacement at global failure, u_f, in the uniaxial tension, plane-strain tension and in-plane shear simulations was reduced when selective-reduced integration or a denser mesh was employed in the FE models, due to a more realistic prediction of the local necking process and crack propagation. It is noted that the prediction of slant fracture in the uniaxial tension and plane-strain tensions simulations had virtually no effect on the global force-displacement curves in Fig. 15. This suggests that the energy dissipated after the onset of shear-band localization in the FE simulations is very small compared to the energy dissipated in local necking, as also discussed by Nielsen and Hutchinson (2011). It is further noted that the uniaxial tension simulation with refined mesh and no softening given in Fig. 15, displays a tendency to slant fracture surface.

Indeed, in a simulation where the ductility parameter W_C was increased to 1400 MPa, slant fracture was predicted, even though no damage softening was included. This increase in W_C did, however, lead to unrealistically large local deformations.

Tensile tests on Docol 600DL specimens with 0.7 mm thickness, but apart from this the same geometry as displayed in Fig. 1, were presented in Rakvåg et al. (2012). They showed that the material behaviour of the 0.7 mm and 2.0 mm thick Docol 600DL sheets was similar. The 0.7 mm thick uniaxial tensile specimens displayed no shear lips and fractured in the through-thickness neck as illustrated in Fig. 16(a) and (c). To see whether the FE models of the uniaxial tension test used in Section 5.3 could predict this behaviour, the models were scaled in the $\mathbf{e}_Z$ direction to obtain 0.7 mm thickness, and run in LS-DYNA. As indicated in Fig. 16(b), through-thickness slant fracture was not predicted in the simulation with damage softening. Fig. 16(c) displays that the in-plane angle between the fracture surface and the $\mathbf{e}_X$ direction in the simulations with dense mesh is in excellent agreement with the experimental data, while the simulation with a coarse mesh does not capture the local necking and the corresponding fracture mode. From this study it is evident that a rather fine mesh is required to capture local necking and the correct fracture mode for the thin-sheet specimens and that damage softening is not necessary to predict this fracture mode.

7 Conclusions

The modified Mohr-Coulomb and the extended Cockcroft-Latham fracture criteria have been used in explicit finite-element simulations of ductile crack propagation in a dual-phase steel sheet. The sheet was discretized with solid elements and the crack propagation was simulated by element erosion. The simulation results were compared to experiments conducted on five different types of specimens (uniaxial tension, plane-strain tension, in-plane shear, 45° and 90° modified Arcan) made from a 2 mm thick Docol 600DL steel sheet. The main conclusion is that the predicted force-displacement curves and crack paths were only to a small degree influenced by the fracture criterion, and it is hard to select one fracture criterion that out-performs the others. It was further found that only small changes in the predicted force-displacement curves and crack paths were obtained when changing from the von Mises to the Hershey yield criterion with a high exponent. However, an improvement of the in-plane crack path in the simulation of the mixed-mode 45° modified Arcan test was achieved by using the

Hershey yield function. The use of selective-reduced integration rather than reduced integration for the eight-node, tri-linear solid elements, or use of a denser mesh in the FE models gave an improved resolution of the large strain gradients in the simulations. This led to predictions of the local necking at a lower actuator displacement as well as a higher crack propagation speed, both of which are in better accordance with the experiments. Slant fracture as observed in the experimental uniaxial tension and plane-strain tension tests was captured in the numerical simulations if material softening was accounted for and a sufficiently refined mesh was used. The prediction of slant fracture did, however, not have any significant effect on the global response as represented by the force-displacement curves.

Acknowledgement

The financial support of this work from the Structural Impact Laboratory (SIMLab), Centre for Research-based Innovation (CRI) at the Norwegian University of Science and Technology (NTNU), is gratefully acknowledged.

References

Areias, P.M., 2006. Analysis of Finite Strain Anisotropic Elastoplastic Fracture in Thin Plates and Shells. Journal of Aerospace Engineering 19, 259.

Avramovic-Cingara, G., Saleh, C.A.R., Jain, M.K., Wilkinson, D.S., 2009. Void Nucleation and Growth in Dual-Phase Steel 600 during Uniaxial Tensile Testing. Metallurgical and Materials Transactions A 40, 3117-3127.

Bai, Y., Wierzbicki, T., 2010. Application of extended Mohr–Coulomb criterion to ductile fracture. International Journal of Fracture 161, 1-20.

Belytschko, T., Liu, W.K., Moran, B., 2000. Nonlinear Finite Elements for Continua and Structures. John Wiley & Sons Ltd.

Bouchard, P.O., Bay, F., Chastel, Y., Tovena, I., 2000. Crack propagation modelling using an advanced remeshing technique. Computer Methods in Applied Mechanics and Engineering 189, 723-742.

Cockcroft, M.G., Latham, D.J., 1968. Ductility and the workability of metals. Journal of the Institute of Metals 96, 33-39.

Curtze, S., 2009. Deformation behavior of TRIP and DP steels in tension at different temperatures over a wide range of strain rates. Materials science & engineering. A, Structural materials 507, 124-131.

de Borst, R., 2004. Damage, Material Instabilities, and Failure. Encyclopedia of Computational Mechanics. Wiley.

Dørum, C., Hopperstad, O.S., Berstad, T., Dispinar, D., 2009. Numerical modelling of magnesium die-castings using stochastic fracture parameters. Engineering Fracture Mechanics 76, 2232-2248.

Fagerholt, E., 2012. Field measurements in mechanical testing using close-range photogrammetry and digital image analysis, 2012:95. PhD thesis, Norwegian University of Science and Technology.

Fagerholt, E., Dørum, C., Børvik, T., Laukli, H.I., Hopperstad, O.S., 2010. Experimental and numerical investigation of fracture in a cast aluminium alloy. International Journal of Solids and Structures 47, 3352-3365.

Fagerström, M., Larsson, R., 2006. Theory and numerics for finite deformation fracture modelling using strong discontinuities. International Journal for Numerical Methods in Engineering 66, 911-948.

Freudenthal, A.M., 1950. The Inelastic Behaviour of Solids. Wiley, New York.

Fyllingen, Ø., Hopperstad, O.S., Langseth, M., 2007. Stochastic simulations of square aluminium tubes subjected to axial loading. International Journal of Impact Engineering 34, 1619-1636.

Gruben, G., Fagerholt, E., Hopperstad, O.S., Børvik, T., 2011. Fracture characteristics of a cold-rolled dual-phase steel European Journal of Mechanics - A/Solids 30, 204-218.

Gruben, G., Hopperstad, O.S., Børvik, T., 2012a. Evaluation of uncoupled ductile fracture criteria for the dual-phase steel Docol 600DL. International Journal of Mechanical Sciences 62, 133-146.

Gruben, G., Vysochinskiy, D., Coudert, T., Reyes, A., Lademo, O.-G., 2012b. Determination of ductile fracture parameters of a dual-phase steel by optical measurements. submitted for possible publication.

Gurson, A.L., 1977. Continuum theory of ductile rupture by void nucleation and growth, 1. Yield criteria and flow rules for porous ductile media. Journal of Engineering Materials and Technology-Transactions of the ASME 99(1), 2-15.

Hershey, A.V., 1954. The Plasticity of an Isotropic Aggregate of Anisotropic Face-Centered Cubic Crystals. Journal Applied Mechanics 76, 241-249.

Hosford, W.F., 1972. A general isotropic yield criterion. Journal of Applied Mechanics 39, 607-609.
Hutchinson, J.W., 1964a. Plastic deformation of b.c.c. polycrystals. Journal of the Mechanics and Physics of Solids 12, 25-33.
Hutchinson, J.W., 1964b. Plastic stress-strain relations of F.C.C polycrystalline metals hardening according to Taylor's rule. Journal of the Mechanics and Physics of Solids 12, 11-24.
Hutchinson, J.W., Tvergaard, V., 1981. Shear band formation in plane strain. International Journal of Solids and Structures 17, 451-470.
Johnsen, T.K., 2009. Fracture of ductile materials: Experiments and simulation. Master thesis, Norwegian University of Science and Technology.
Johnson, G.R., Cook, W.H., 1985. Fracture characteristics of three metals subjected to various strains, strain rates, temperatures and pressures. Engineering Fracture Mechanics 21, 31-48.
Kane, A., Børvik, T., Berstad, T., Benallal, A., Hopperstad, O.S., 2011. Failure criteria with unilateral conditions for simulation of plate perforation. European Journal of Mechanics - A/Solids 30, 468-476.
Kazutake, K., 1999. Simulation of chevron crack formation and evolution in drawing. International Journal of Mechanical Sciences 41, 1499-1513.
Komori, K., 2005. Ductile fracture criteria for simulating shear by node separation method. Theoretical and Applied Fracture Mechanics 43, 101-114.
Lemaitre, J., 1992. A course on Damage Mechanics. Springer-Verlag.
Lemaitre, J., Chaboche, J.-L., 1990. Mechanics of solid materials. Cambridge University Press. Cambridge, UK
Li, Y., Wierzbicki, T., Sutton, M., Yan, J., Deng, X., 2011. Mixed mode stable tearing of thin sheet AI 6061-T6 specimens: experimental measurements and finite element simulations using a modified Mohr-Coulomb fracture criterion. International Journal of Fracture 168, 53-71.
Lode, W., 1926. Versuche über den Einfluß der mittleren Hauptspannung auf das Fließen der Metalle Eisen, Kupfer und Nickel. Zeitschrift für Physik A Hadrons and Nuclei 36, 913-939.
LSTC, 2007. LS-DYNA keyword user's manual, version 971. Livermore Software Technology Corporation, US-CA
MATLAB, 2009. version 7.9 (R2009b). The MathWorks Inc., US-MA
Mediavilla, J., Peerlings, R.H.J., Geers, M.G.D., 2006. A robust and consistent remeshing-transfer operator for ductile fracture simulations. Computers & Structures 84, 604-623.
Needleman, A., 1988. Material rate dependence and mesh sensitivity in localization problems. Computer Methods in Applied Mechanics and Engineering 67, 69-85.
Needleman, A., 1990. An analysis of decohesion along an imperfect interface. International Journal of Fracture 42, 21-40.
Needleman, A., Tvergaard, V., 1992. Analyses of Plastic Flow Localization in Metals. Applied Mechanics Reviews 45, S3-S18.
Nielsen, K.L., Hutchinson, J.W., 2011. Cohesive traction–separation laws for tearing of ductile metal plates. International Journal of Impact Engineering 48, 15-23.
Rakvåg, K.G., Underwood, N., Schleyerb, G.K., Børvik, T., Hopperstad, O.S., 2012. Transient pressure loading of plates with pre-formed holes. International Journal of Impact Engineering. http://dx.doi.org/10.1016/j.ijimpeng.2012.07.013.
Rousselier, G., 1987. Ductile fracture models and their potential in local approach of fracture. Nuclear Engineering and Design 105, 97-111.

Shima, S., Oyane, M., 1976. Plasticity theory for porous metals. International Journal of Mechanical Sciences 18, 285-291.

Solberg, J.K., Leinum, J.R., Embury, J.D., Dey, S., Børvik, T., Hopperstad, O.S., 2007. Localised shear banding in Weldox steel plates impacted by projectiles. Mechanics of Materials 39, 865-880.

SSAB, 2009. Docol DP/DL Cold reduced dual phase steels. http://www.ssab.com/Global/DOCOL/datasheets_docol/en/201_Docol%20DP%20DL.pdf, [cited: 27.04.2012]

Tarigopula, V., Langseth, M., Hopperstad, O.S., Clausen, A.H., 2006. Axial crushing of thin-walled high-strength steel sections. International Journal of Impact Engineering 32, 847-882.

Tvergaard, V., 2001. Crack growth predictions by cohesive zone model for ductile fracture. Journal of the Mechanics and Physics of Solids 49, 2191-2207.

Tvergaard, V., Hutchinson, J.W., 1996. Effect of strain-dependent cohesive zone model on predictions of crack growth resistance. International Journal of Solids and Structures 33, 3297-3308.

Wilkins, M.L., Streit, R.D., Reaugh, J.E., 1980. Cumulative-strain-damage model of ductile fracture: simulation and prediction of engineering fracture tests, Technical Report UCRL-53058. Lawrence Livermore National Laboratory.

Xue, L., Wierzbicki, T., 2008. Ductile fracture initiation and propagation modeling using damage plasticity theory. Engineering Fracture Mechanics 75, 3276-3293.

Table 1 Chemical composition of Docol 600DL (in wt. %),(SSAB, 2009).

C	Si	Mn	P	S	Al_{tot}
0.10	0.40	1.50	0.010	0.002	0.040

Table 2 Characteristic initial element size used in the FE models with coarse and fine discretization (in mm).

Uniaxial tension	Plane-strain tension	In-plane shear	Modified Arcan
0.38	0.37	0.13	0.31
0.084	0.078	0.077	—

Table 3 Parameters in the rate-dependent extended Voce hardening model in the uncoupled (top row) and coupled (bottom row) damage model. The high value of $\dot{\varepsilon}_0$ is due to time-scaling.

σ_0 [MPa]	Q_1 [MPa]	C_1	Q_2 [MPa]	C_2	Q_3 [MPa]	C_3	$\dot{\varepsilon}_0$ [s^{-1}]	q
286.2	287.9	34.93	341.1	5.00	6000	0.01	100	0.005
287.1	297.1	33.72	339.4	4.63	6000	0.01	100	0.005

Table 4 Calibrated fracture parameters for Docol 600DL.

Fracture criterion	C [MPa]	W_C [MPa]	ϕ	γ
Modified Mohr-Coulomb ($m = 2$)	1037	—	0.208	—
Modified Mohr-Coulomb ($m = 8$)	1033	—	0.078	—
Extended Cockcroft-Latham ($m = 2$)	—	815	0.335	1.55
Extended Cockcroft-Latham ($m = 6$)	—	886	0.192	3.02
Extended Cockcroft-Latham ($m = 8$)	—	1035	0.0884	5.75
Cockcroft-Latham ($m = 2$)	—	725	1.000	1.00
Cockcroft-Latham ($m = 8$)	—	722	1.000	1.00
Integral-based Tresca ($m = 2$)	—	834	0.000	1.00
Integral-based Tresca ($m = 8$)	—	801	0.000	1.00
ECL, dense mesh ($m = 2,\ \beta = \infty$)	—	888	0.335	1.55
ECL, dense mesh ($m = 2,\ \beta = 6$)	—	1033	0.335	1.55

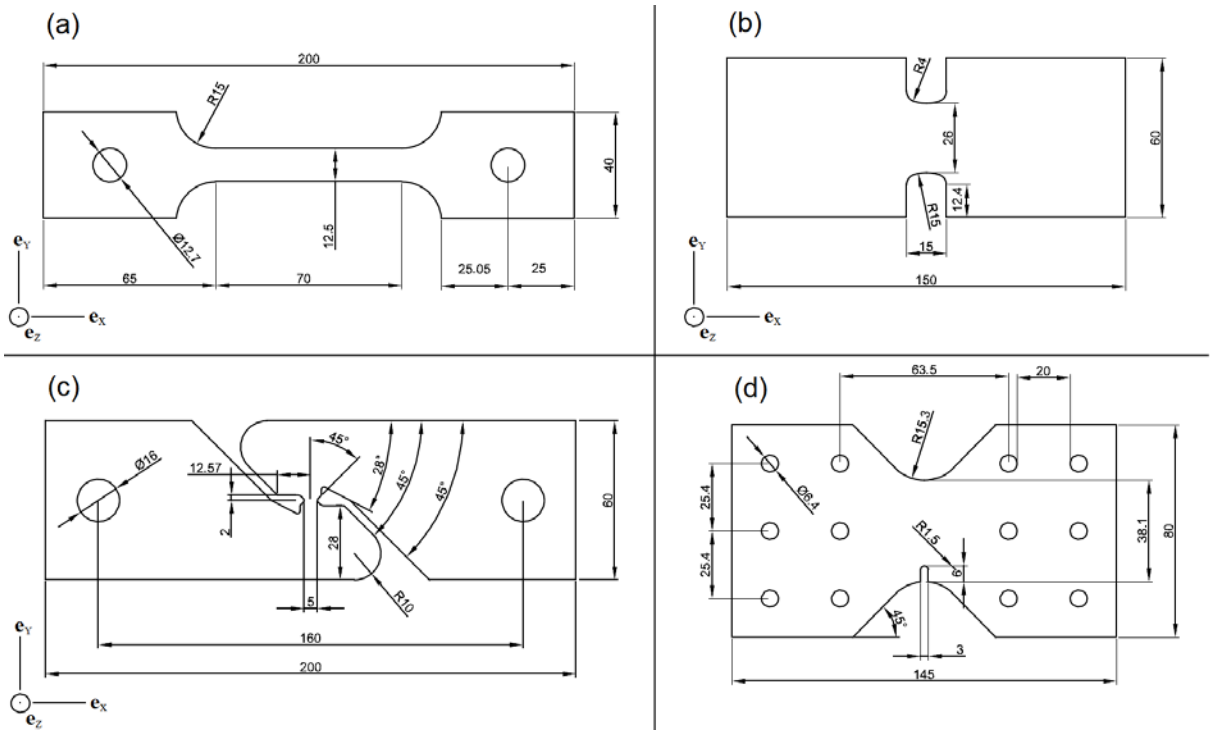

Fig. 1 Geometry of the test specimens (in mm): (a) uniaxial tension, (b) plane-strain tension, (c) in-plane shear, and (d) modified Arcan (Gruben et al., 2011).

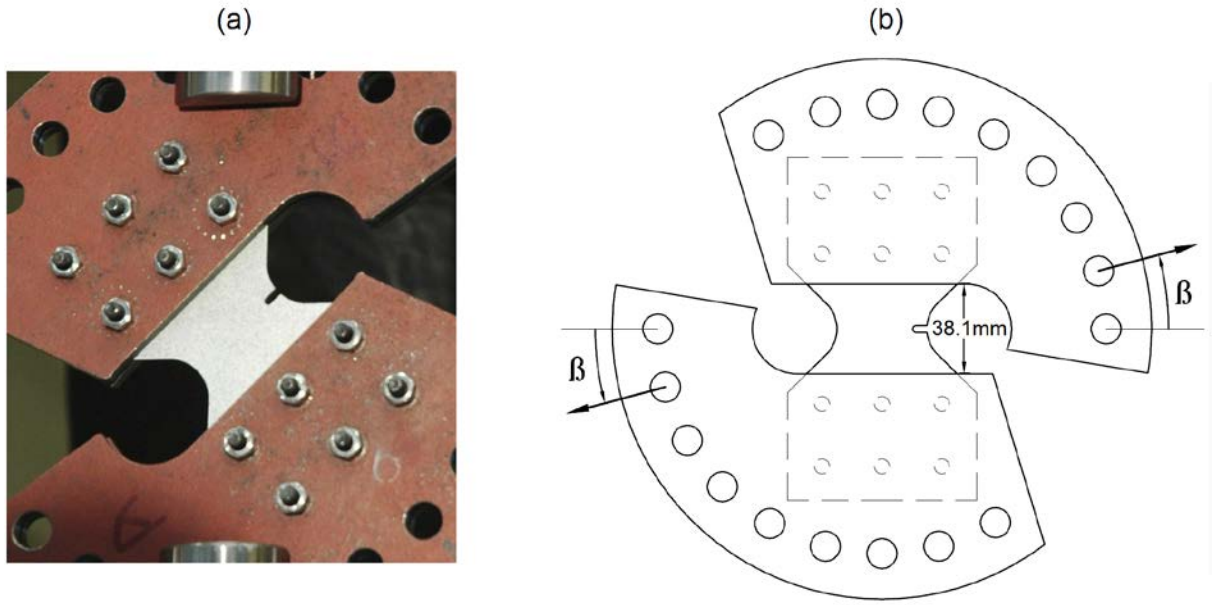

Fig. 2 (a) Modified Arcan test set-up with $\beta = 45°$, and (b) sketch of brackets with specimen defining the loading direction β (Gruben et al., 2011).

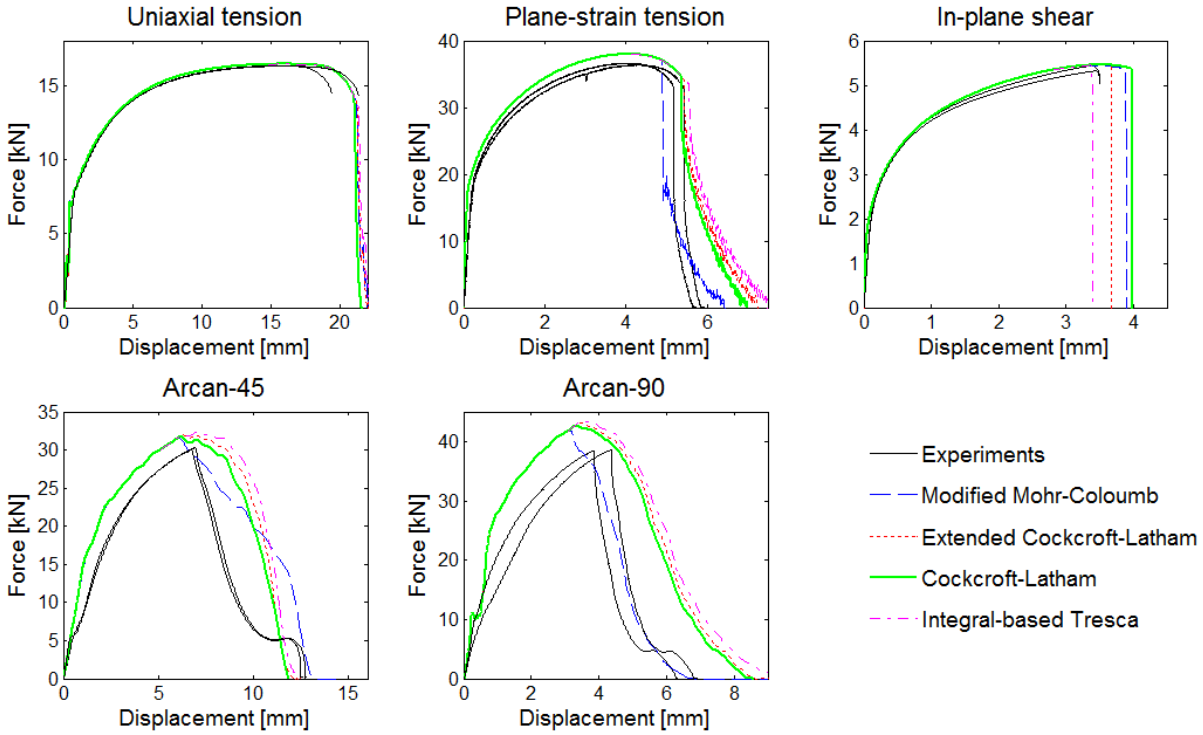

Fig. 3 Force-displacement curves from experiments and simulations with J_2 flow theory and the four fracture criteria.

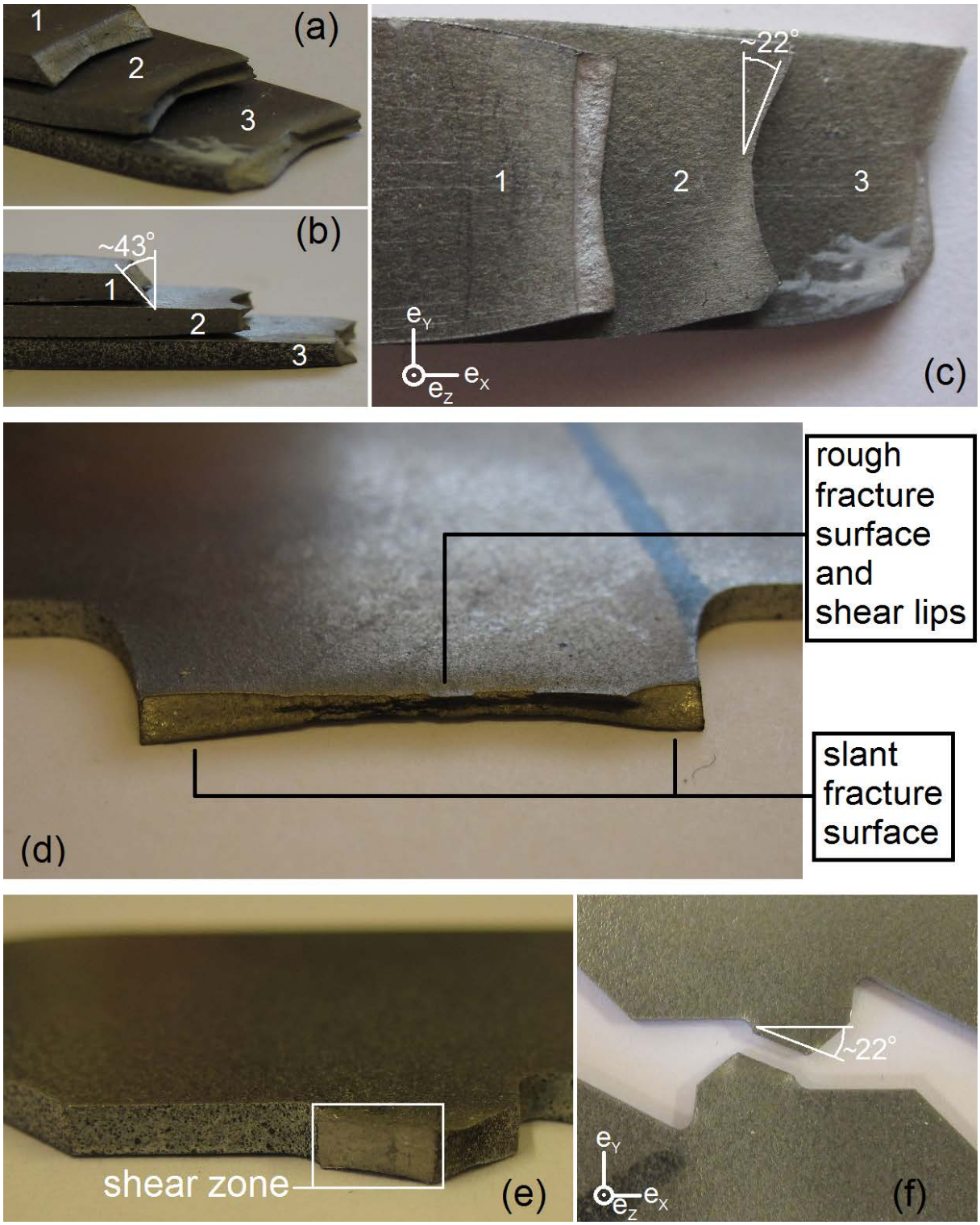

Fig. 4 Pictures (a), (b) and (c) display the three different modes of fracture in the uniaxial tension tests, where "1" is the slant fracture, "2" is the V-mode and "3" is a combination of "1" and "2". Picture (d) shows fracture in the plane-strain tension test, while picture (e) and (f) illustrate fracture in the in-plane shear test.

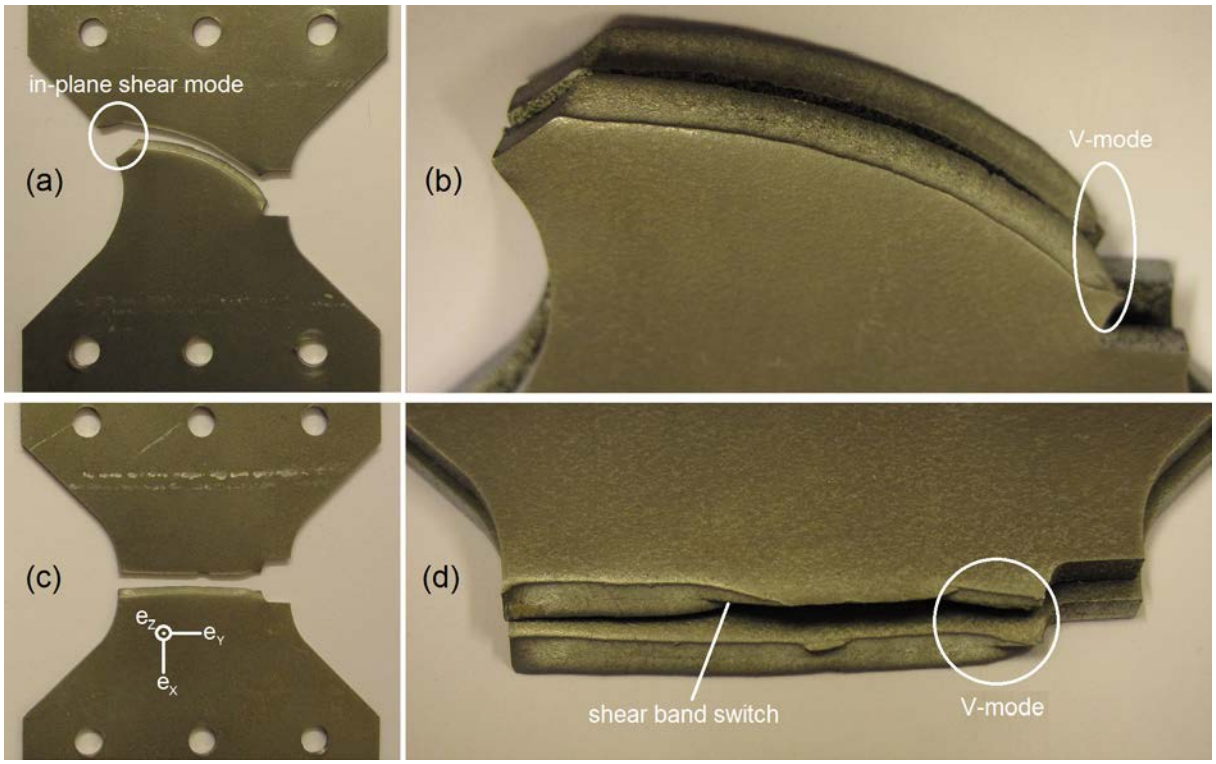

Fig. 5 Pictures (a) and (b) display fracture of the Arcan-45 tests. Fracture started in a V-mode and then propagated in a slant fracture mode before the crack got arrested and finally ended in a flat shear mode. Pictures (c) and (d) display fracture of the Arcan-90 tests, where fracture initiated in a V-mode and continued in a slant fracture mode to global failure.

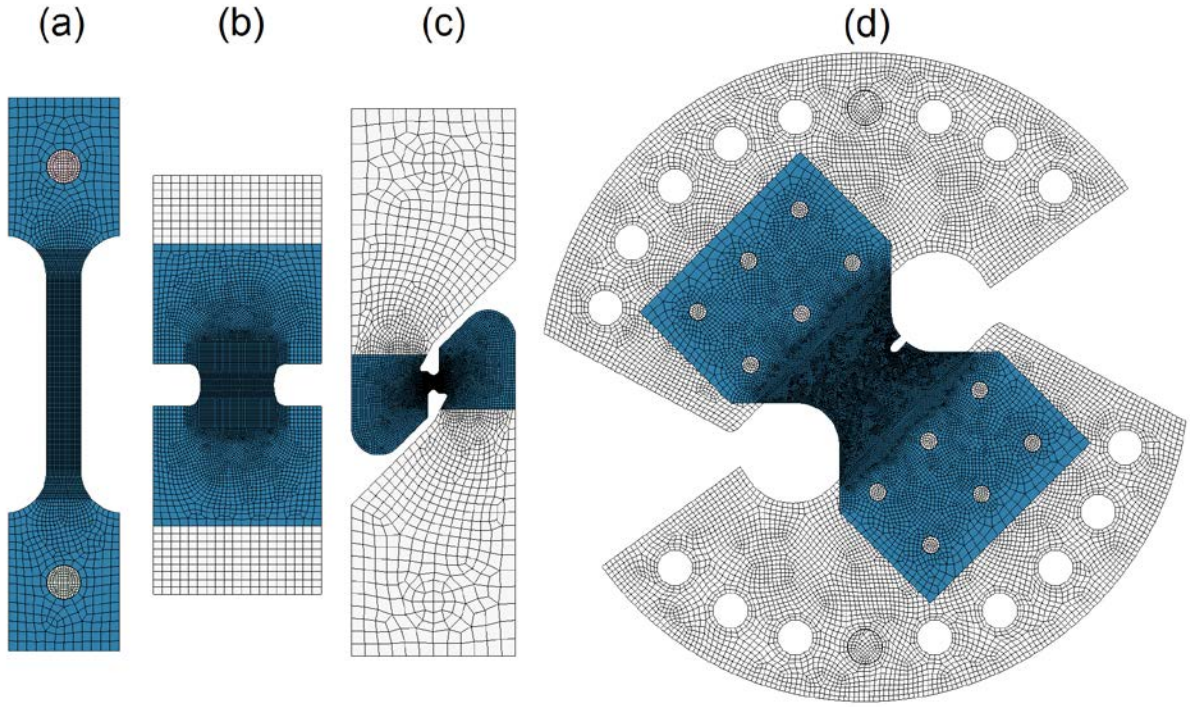

Fig. 6 Finite element meshes of the test specimens: (a) uniaxial tension, (b) plane-strain tension, (c) in-plane shear and (d) modified Arcan.

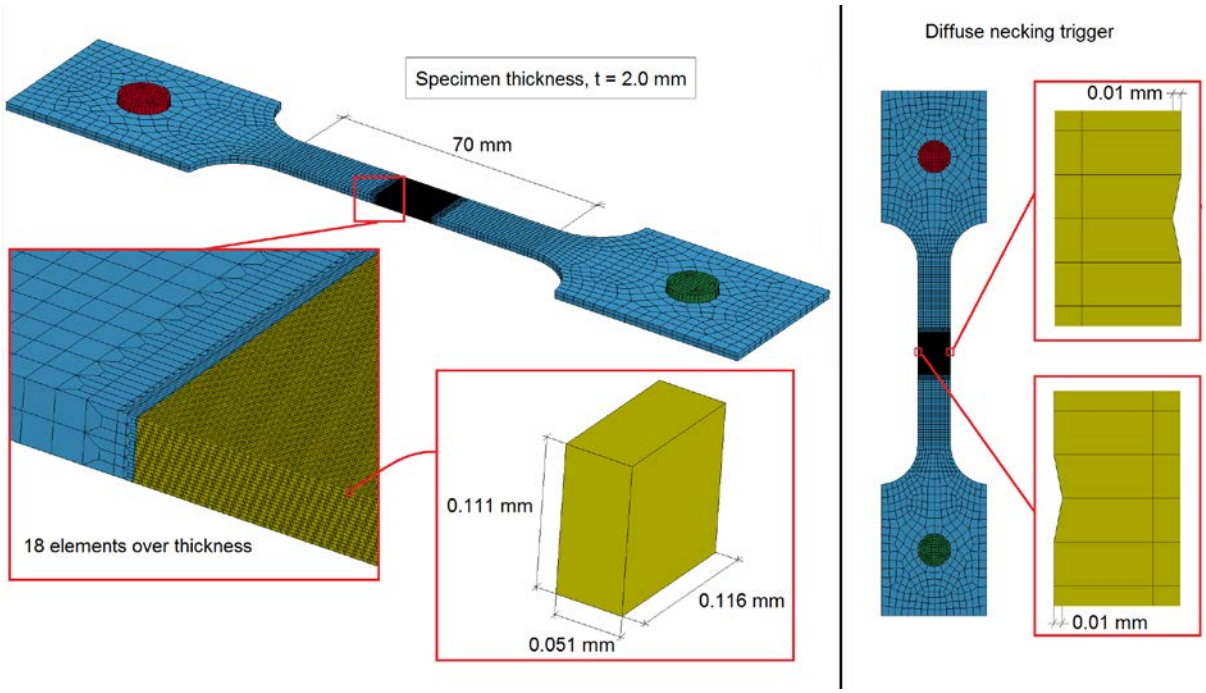

Fig. 7 Discretization of uniaxial tension specimen with dense mesh.

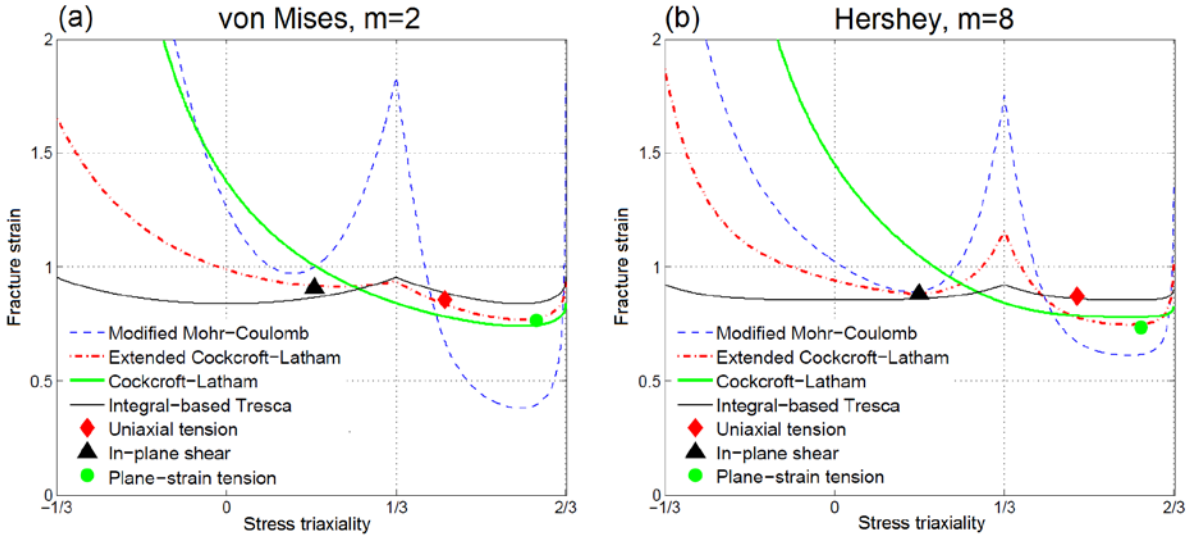

Fig. 8 Calibrated fracture locus $(\sigma^*, \bar{\varepsilon}_f^p)$ for the various fracture criteria under the assumption of proportional loading and plane stress. (a) J_2 flow theory $(m = 2)$, and (b) Hershey yield surface $(m = 8)$. The $(\sigma^*_{\text{avg}}, \bar{\varepsilon}_f^p)$ values for the three tests used in calibration of the ECL criterion are also plotted.

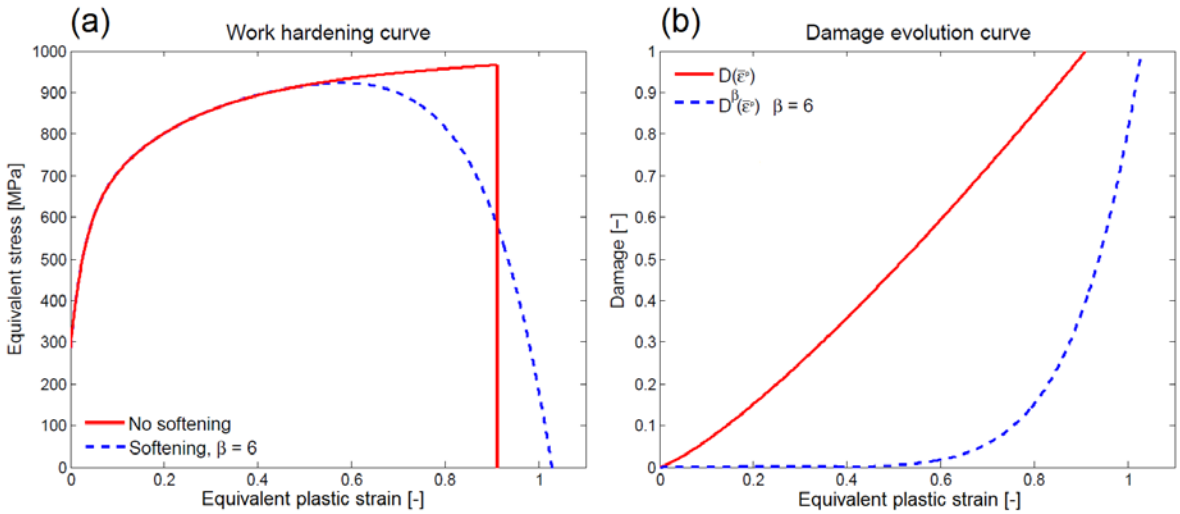

Fig. 9 (a) Work-hardening curves for uncoupled and coupled damage. The plastic work (area under the curves) is the same. (b) Damage evolution as function of equivalent strain without weakening exponent, $D(\bar{\varepsilon}^p)$, and width weakening exponent $D^\beta(\bar{\varepsilon}^p)$.

Fig. 10 Crack paths in simulations of different specimens with the four fracture criteria using J_2 flow theory. From top: uniaxial tension, plane-strain tension, in-plane shear, Arcan-45 and Arcan-90. The contours are equivalent plastic strain, and the displacement u corresponding to the given plot is marked in each case.

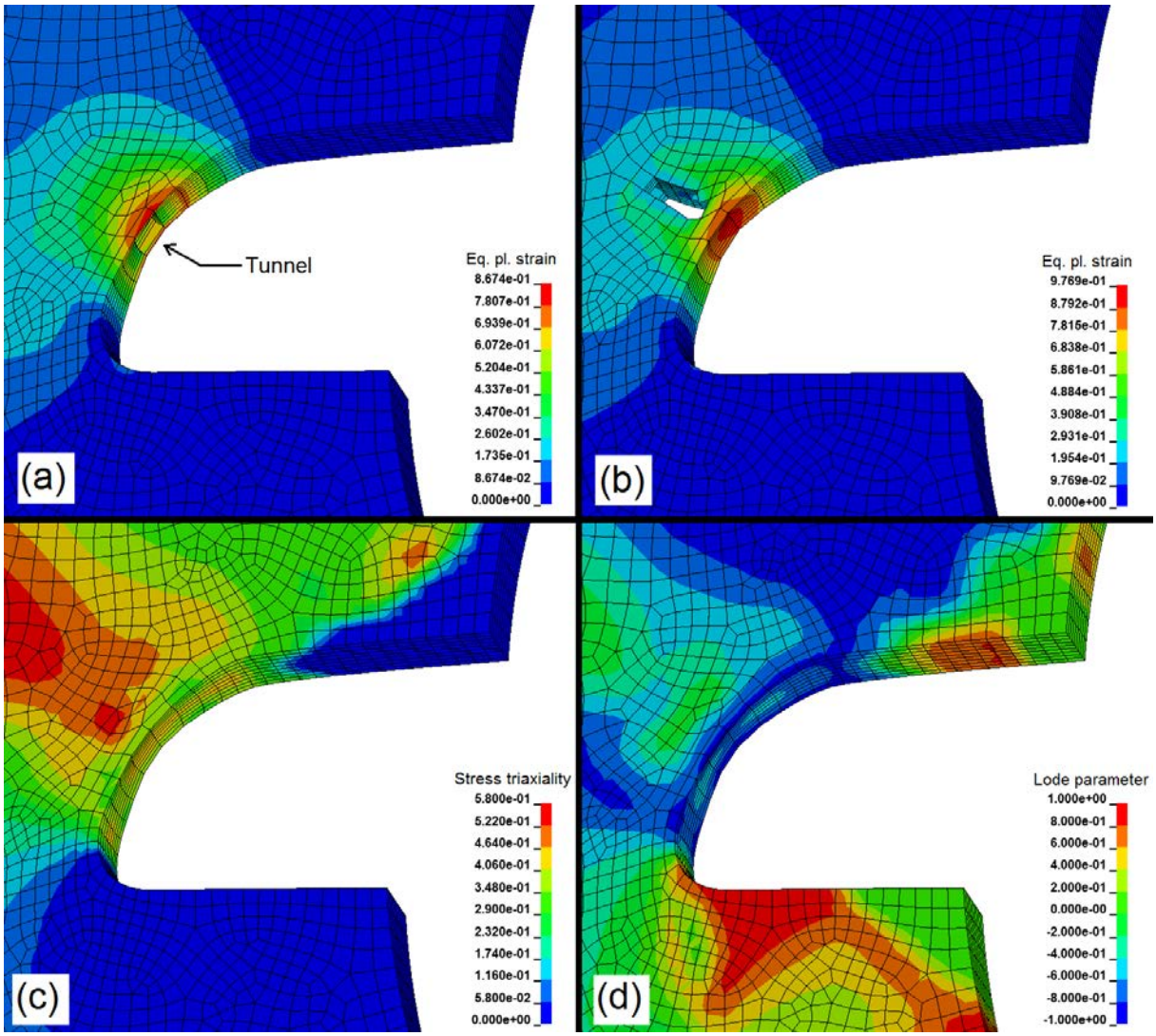

Fig. 11 Fracture initiation in Arcan-45 simulations: (a) Tunnelling effect observed in simulation with the ECL criterion and (b) elements eroded at a certain distance away from the expected fracture initiation point with the MMC criterion, (c) and (d) give the contour plots of respectively the stress triaxiality and the Lode parameter just before the first element is eroded in the simulation with the MMC criterion.

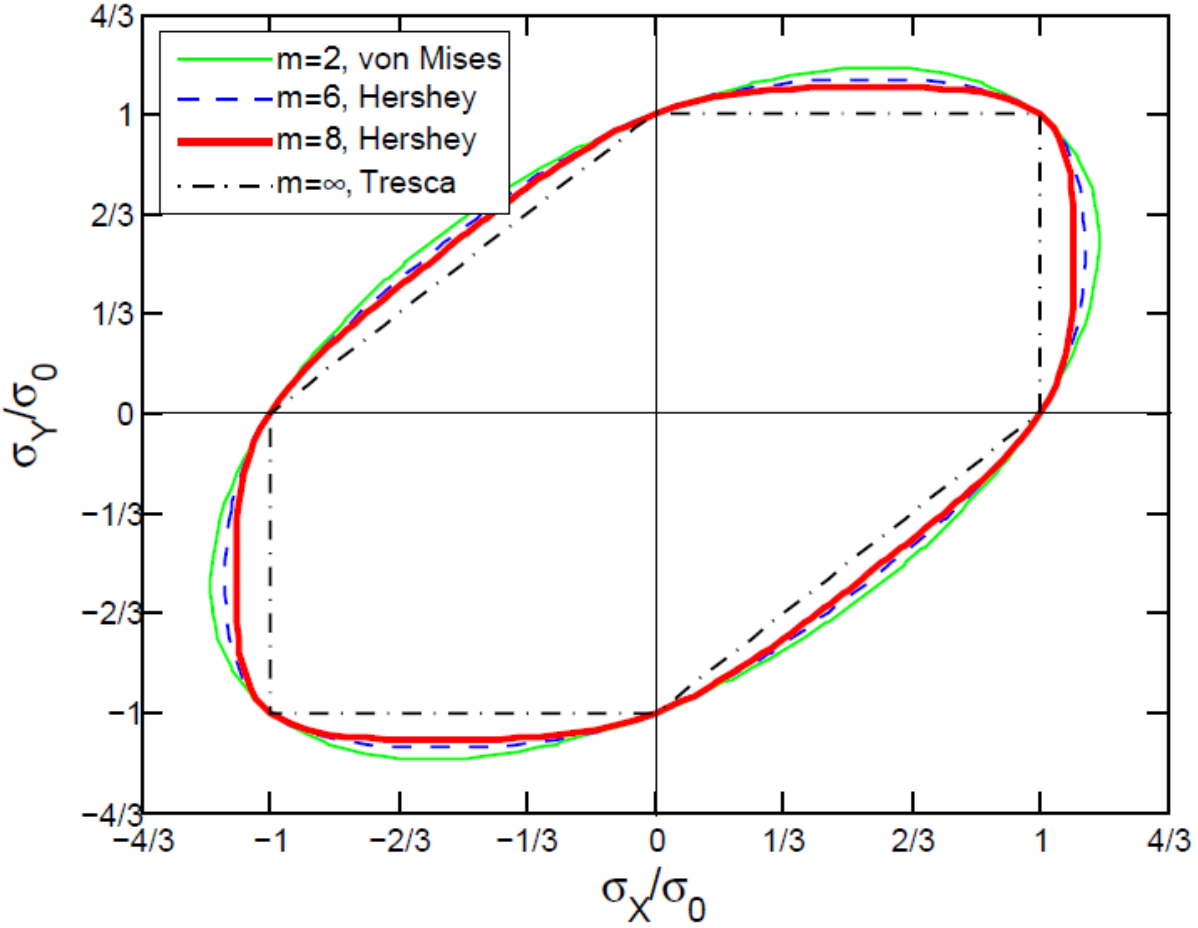

Fig. 12 Normalized yield loci obtained with the von Mises, Hershey and Tresca yield function.

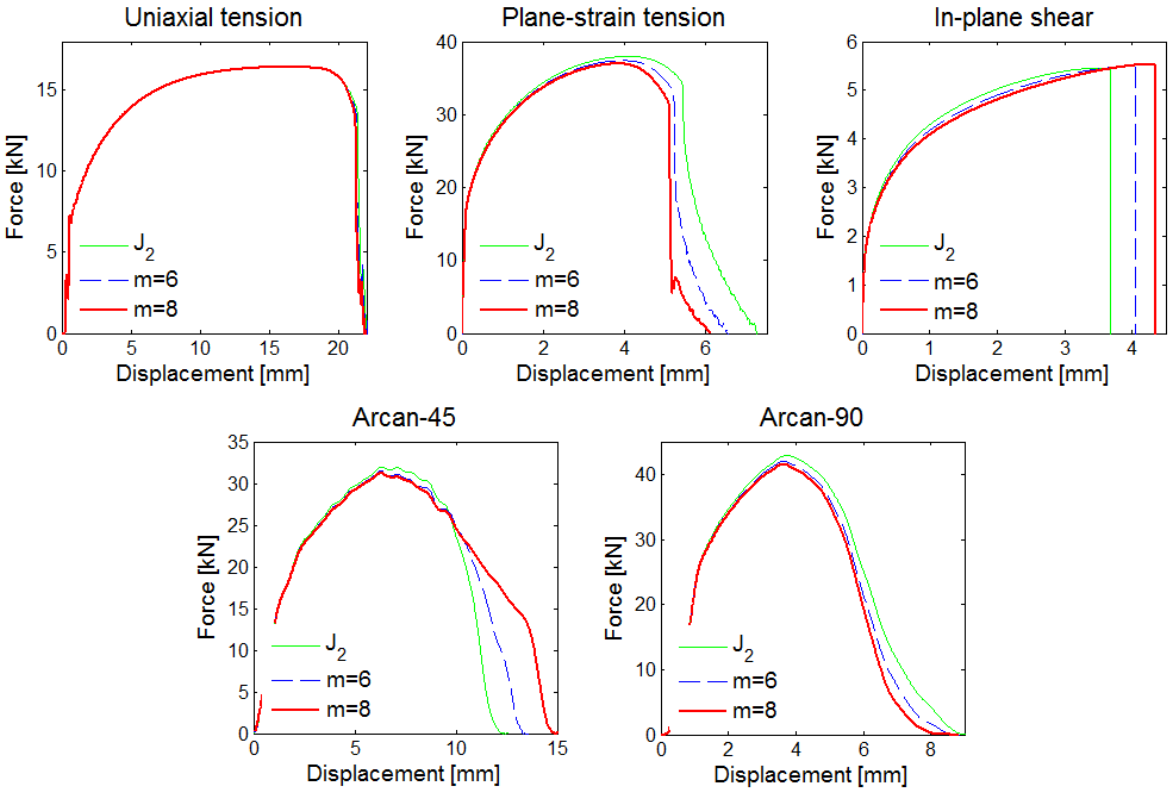

Fig. 13 Force-displacement curves from experiments and simulations using the extended Cockcroft-Latham criterion and yield functions with different *m* values.

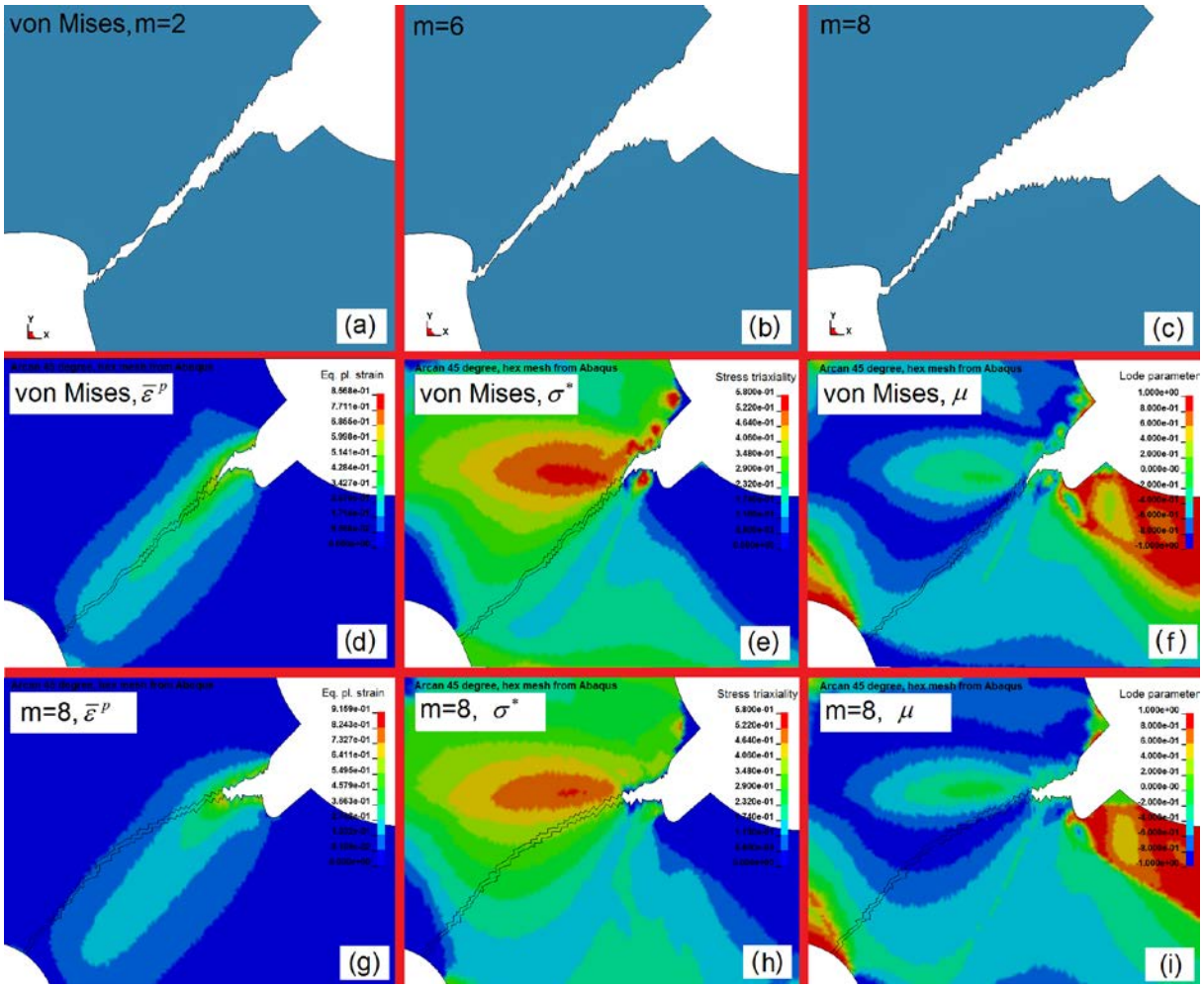

Fig. 14 Plots (a)-(c) display the effect of the yield function on the crack path in the Arcan-45 simulations. Plots (d)-(i) present contours of $\bar{\varepsilon}^p$, σ^* and μ in the early stages of fracture in the Arcan-45 simulations with: (d)-(f) J_2 flow theory and (g)-(i) Hershey yield function $(m = 8)$. The subsequent crack path is marked in plots (d)-(i).

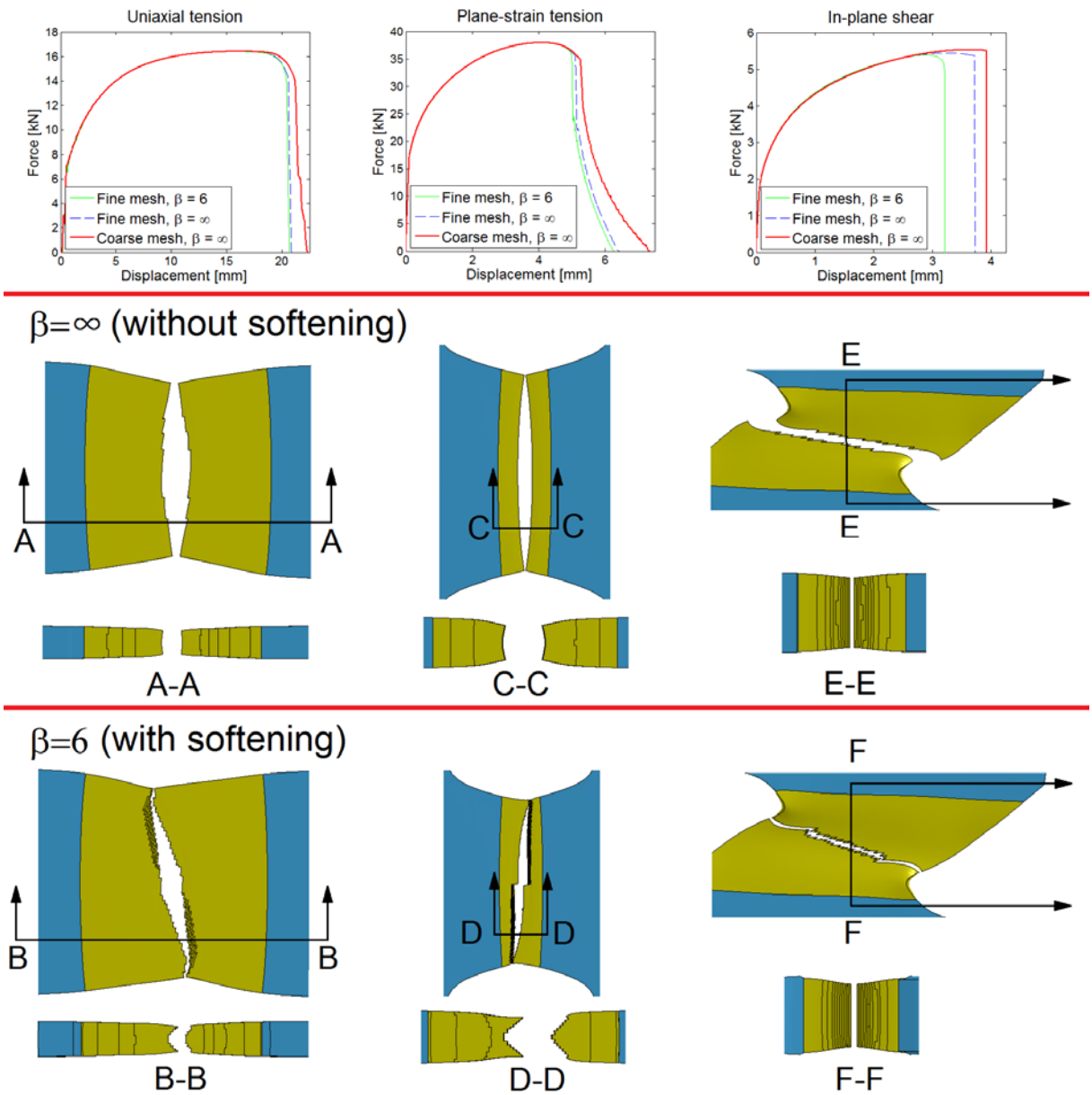

Fig. 15 Force-displacement curves in FE analyses with coarse and dense mesh without softening and dense mesh with softening. The crack surfaces are from simulations with dense mesh, with and without softening.

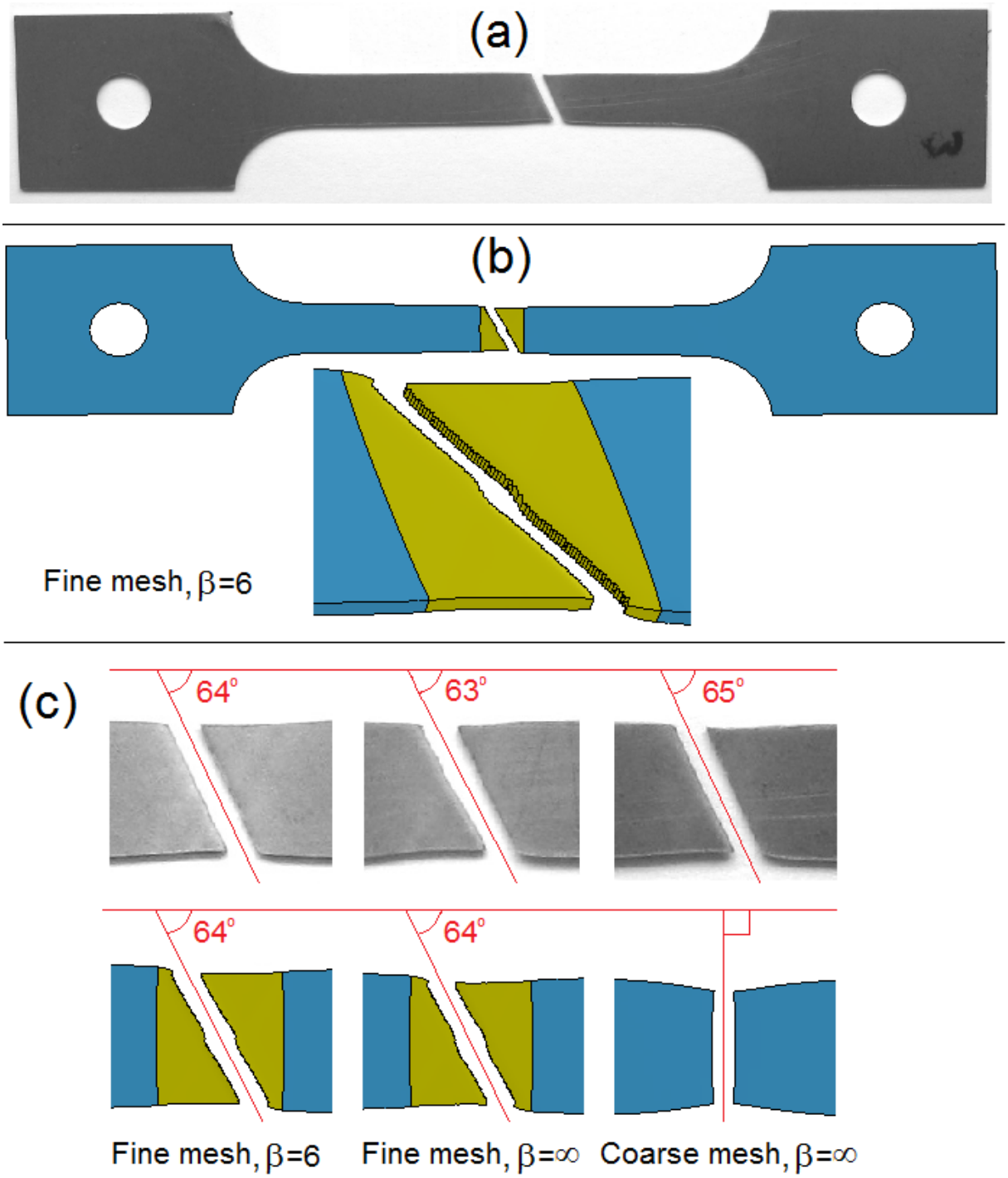

Fig. 16 Experiments and FE simulations of tensile tests on 0.7 mm thick specimens. (a) Failed specimen in experiment, (b) failed specimen and fracture surface in FE simulation with coupled damage. (c) In-plane angles of fracture surface in three parallel tests and in FE simulations with different mesh density and coupled/uncoupled damage.